# Stability and Sensitivity Limit of a Few-Photon Homodyne Interferometer for Yb Quantum Optics Experiments

Theresa Dewey

Bachelorarbeit in Physik
angefertigt im Institut für Angewandte Physik

vorgelegt der
Mathematisch-Naturwissenschaftlichen Fakultät
der
Rheinischen Friedrich-Wilhelms-Universität
Bonn

April 2024

Ich versichere, dass ich diese Arbeit selbstständig verfasst und keine anderen als die angegebenen Quellen und Hilfsmittel benutzt sowie die Zitate kenntlich gemacht habe.

Bonn, 03.04.2024
Datum

Theresa Dewey
Unterschrift

1. Gutachter: Prof. Dr. Sebastian Hofferberth
2. Gutachter: Dr. Frank Vewinger

# Contents

CHAPTER 1

# Introduction

Being able to control photon-photon interactions is a goal many experiments are working towards for further developing quantum communication and quantum technologies. While in free space those interactions are negligible, it is possible to generate them with the help of a mediator, a nonlinear medium. Multiple Nonlinear Quantum Optics experiments around the world use highly excited Rydberg atoms to mediate the interaction between single photons. Using the Rydberg blockade mechanism, the dense cloud of ultracold atoms exhibits properties of a strongly nonlinear medium for few-photon pulses that are sent through [1]. This nonlinearity generates an effective photon-photon interaction that can be used for interesting quantum technology applications, such as photon-photon logic gates [2].

In the Ytterbium Quantum Optics (YQO) laboratory at the University of Bonn, we use ultracold $^{174}$Yb Rydberg atoms to generate strong photon-photon interactions. The atoms are cooled and trapped at high densities in an optical dipole trap inside an ultra-high vacuum science chamber [3]. Rydberg polaritons are then generated using electromagnetically induced transmission with a two-photon excitation scheme, which creates the strong nonlinearity of the medium and thus the effective interaction for the single photons sent through the science chamber.

To investigate and optimize the generation of photon-photon interactions it is essential to measure the effect of the Ytterbium Rydberg medium on the photons that cross it. Observing bunching or anti-bunching of these photons is possible by measuring time correlations of single-photon detections. This is commonly executed with a Hanbury-Brown-Twiss (HBT) setup and provides information on the photon statistics but not on the phase. The phase information can be acquired by using interferometric measurements. A powerful example on measuring the phase of a quantum state is homodyne detection [4].

The homodyne detection method is based on a Mach-Zehnder interferometer where the two interferometer arms are strongly unbalanced in terms of their optical power. The weaker arm, called probe beam, runs in the few-photon regime and is sent through the nonlinear medium while the stronger arm works as a phase reference and is guided around the science chamber. This arm is called local oscillator (LO) and is of the same frequency as the probe arm. The two outputs of the interferometer display the interference of the two interferometer arms and are detected on a balanced photodetector which also subtracts the two signals. A perfectly balanced beamsplitter at the output leads to the suppression of the local oscillator noise and results in a homodyne detection signal of low noise which

is centered around zero. Phase fluctuations of the photons from the probe beam are then visible because of the interference with the strong LO beam. Scanning the phase of the local oscillator and measuring the fluctuations of the signal in the time-domain makes it possible to reconstruct the density matrix and Wigner functions of the probe photons and thus obtaining their full quantum state [5, 6].

In addition to the existing HBT setup of the YQO experiment in Bonn that is measuring the time correlations of photons crossing the science chamber, a new homodyne detection setup was designed and recently built based on a setup developed by the group of Alexei Ourjoumtsev [7]. As the Ytterbium 399 nm transition requires light in the visible spectrum, challenges occured performing the change from infrared to blue light. Some of those challenges were conquered in the build-up and first characterization of the interferometer setup in the YQO laboratory [8]. Building on the first iteration of the setup, during this thesis project I worked on bringing the setup to the next stage aiming for the implementation into the main YQO experiment.

In this thesis I present the work I have done to characterize and optimize the phase stability of the new homodyne setup. In chapter 3 the process of determining the phase stability is described. Extracting the phase out of measurements in the time-domain can be performed by using the method of the Hilbert transform on which I will elaborate further in subsection 3.1.1. Following the characterization of the phase stability I aimed to stabilize the interferometer by making different additions and changes to the setup. To find out if the homodyne signal is still visible for very low photon rates I measured the signal-to-noise ratio of the interference signal of the setup in chapter 4. Additionally, I investigated whether changing of certain parameters would increase the signal-to-noise ratio leading to an improved detection limit of the setup which I discussed in section 4.4.

CHAPTER 2

# Homodyne interferometry

The phenomenon of interference was first discovered with the double slit experiments, observing a multispot pattern with well-defined spacings between the bright spots. The so far known classical picture would have only predicted two spots on the observation screen. Treating the coherent light as a wave with a certain phase, it becomes clear how the difference in path lengths of two light beams also leads to a phase difference between the interfering waves. This phase difference causes constructive and destructive interference depending on the observation position which sets the path length for both beams and thus the difference in phases. In interferometers, the interference is not visible in a 2D-pattern on a screen but is measured in one dimension with the help of intensity sensitive devices like photodiodes. The aim of this chapter will be to give an overview over the mechanisms and the quantum mechanical descriptions of homodyne detection as well as an introduction into the experimental setup.

## 2.1 Balanced homodyne detection

Homodyne detection is a method to extract phase components of free-propagating photons. A laser beam is split up on a beamsplitter and the two output beams interfere in a Mach-Zehnder-Interferometer. In contrast to heterodyne interferometry, where a beat signal is created by the interference of light of two different frequencies, in homodyne interferometry both interfering beams are of the same frequency and thus no interference fringes should be visible when overlapping them on a beamsplitter. Since homodyne detection is a tool to work with single photons, the probe beam on one of the beamsplitter inputs is very weak compared to the local oscillator. In balanced homodyning the overlap happens on a 50:50 beamsplitter so both output beams of the interferometer are of the same light intensity. A sketch of the detection setup is shown in Figure 2.1. It is especially interesting to observe the difference between the two measured intensities. In the case of perfect balancing and no phase differences between the two arms the difference is zero. Measuring a difference signal varying from zero provides information about the different phase shifts of the light in the two arms of the interferometer.

The two intensities $\hat{I}$ can be expressed in operator form as the product of the creation $\hat{a}'^{\dagger}_{1,2}$ and annihilation $\hat{a}'_{1,2}$ operators of the respective output beam. Taking the expectation value gives the intensity $I_{1,2}$ detected on each photodiode. Following the calculations in [4] subtracting the intensities measured

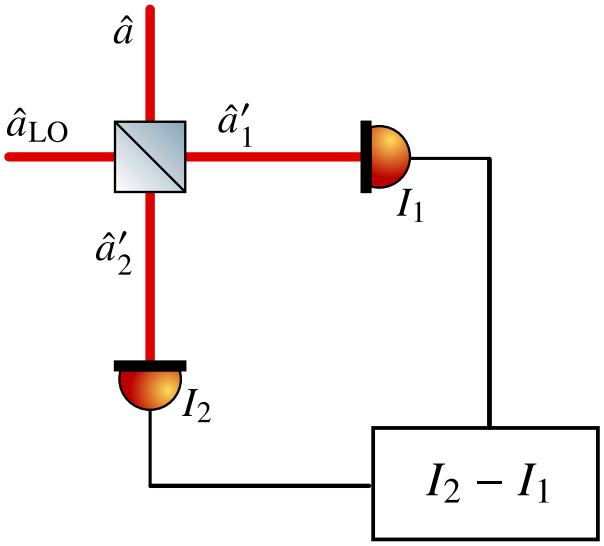


Figure 2.1: Ideal homodyne detection setup: The probe beam $\hat{a}$ and the local oscillator $\hat{a}_{\mathrm{LO}}$ are overlapped on a equally splitting beamsplitter and the output intensities $I_{1,2}$ are measured on two photodiodes. These intensities are electronically subtracted and also observed.

on the two photodiodes after the beamsplitter leads to

$$\Delta\hat{I} = \hat{I}_2 - \hat{I}_1 = \hat{a}_2'^{\dagger}\hat{a}_2' - \hat{a}_1'^{\dagger}\hat{a}_1' = \hat{n}_{12}. \tag{2.1}$$

The expectation value of this number operator $\hat{n}_{12}$ is a measure for the balancing between the two output beams of the interferometer since it is zero for two beams that are split up 50:50 and propagate in phase.

Assuming the LO to be in a coherent state and sufficiently high in intensity, we can treat the beam classically and write the annihilation operator $\hat{a}_{\mathrm{LO}}$ as the complex amplitude $\alpha_{\mathrm{LO}}$

$$\hat{a}_{\mathrm{LO}} \rightarrow \alpha_{\mathrm{LO}} = |\alpha_{\mathrm{LO}}|e^{i\vartheta}, \tag{2.2}$$

where the angle $\vartheta$ is the phase of the local oscillator. The probe beam still has to be described by the respective operators $\hat{a}$ and $\hat{a}^{\dagger}$. Taking the beamsplitter operations

$$\begin{aligned} \hat{a}_1' &= \frac{1}{\sqrt{2}}(\hat{a} + \hat{a}_{\mathrm{LO}}) \\ \hat{a}_2' &= \frac{1}{\sqrt{2}}(\hat{a} - \hat{a}_{\mathrm{LO}}) \end{aligned} \tag{2.3}$$

into account, the difference signal operator $\Delta\hat{I}$ is obtained as

$$\begin{aligned} \Delta\hat{I} &= \hat{a}\hat{a}_{\mathrm{LO}}^{\dagger} + \hat{a}^{\dagger}\hat{a}_{\mathrm{LO}} \\ &= |\alpha_{\mathrm{LO}}|(\hat{a}e^{-i\vartheta} + \hat{a}^{\dagger}e^{i\vartheta}). \end{aligned} \tag{2.4}$$

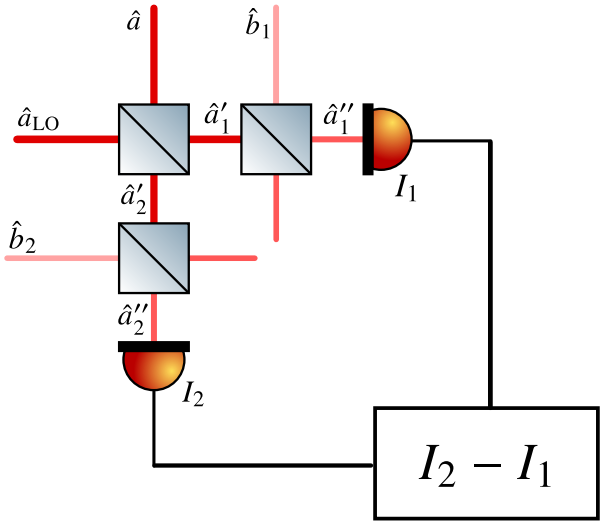


Figure 2.2: Simulation of a real homodyne detector by including additional beamsplitters before the detection area of the photodetector. By the mixing with the vacuum inputs $\hat{b}_{1,2}$ on the second beamsplitters of transmission $\eta$, the two signals experience losses corresponding to the efficiency limits of the real detection setup.

Writing this quantity by using the quadrature $\hat{X}(\vartheta)$ known as $\hat{X}(\vartheta) = \frac{1}{\sqrt{2}}(\hat{a}e^{-i\vartheta} + \hat{a}^\dagger e^{i\vartheta})$ one finds

$$\Delta\hat{I} = \sqrt{2}\,|\alpha_{\mathrm{LO}}|\hat{X}(\vartheta). \tag{2.5}$$

From the equations derived above we can refer the measured difference signal to the information about the quadratures of the light.

While this simple formula can be obtained by the assumption of a perfect photodetector, different sources of losses induced in the real setup such as a certain quantum efficiency $< 1$ or mismatch of modes can change the behavior of the interference signal. These losses can be simulated by the interaction of the beams with the vacuum operators $\hat{b}_{1,2}$ of the inputs of additional imagined beamsplitters with a transmission of $\eta$ before hitting the photodiodes sketched in Figure 2.2. This $\eta$ can be chosen such that it will take the different losses in the setup into account and it is possible to derive a calculation for the actually measured intensities instead of only the ideal case. After passing the two additional beamsplitters the annihilation operators of the two output beams of the 50:50 beamsplitter at the beginning of the interferometer $\hat{a}'_{1,2}$ are transformed to

$$\hat{a}''_{1,2} = \sqrt{\eta}\,\hat{a}'_{1,2} + \sqrt{1-\eta}\,\hat{b}_{1,2}. \tag{2.6}$$

Due to these additional losses also the difference in intensities will change. The intensities measured on the two detectors will now be described by $\hat{I}_1 = \hat{a}_1''^\dagger \hat{a}''_1$ and $\hat{I}_2 = \hat{a}_2''^\dagger \hat{a}''_2$ and their difference by

$$\begin{aligned}\Delta\hat{I} = &(\sqrt{\eta}\,\hat{a}_2'^\dagger + \sqrt{1-\eta}\,\hat{b}_2^\dagger)\,(\sqrt{\eta}\,\hat{a}'_2 + \sqrt{1-\eta}\,\hat{b}_2)\\ &-(\sqrt{\eta}\,\hat{a}_1'^\dagger + \sqrt{1-\eta}\,\hat{b}_1^\dagger)\,(\sqrt{\eta}\,\hat{a}'_1 + \sqrt{1-\eta}\,\hat{b}_1).\end{aligned} \tag{2.7}$$

Using the beamsplitter operations from Equation 2.3 again and assuming the local oscillator to be much stronger than the weak beam and coherent as before, this equation simplifies to

$$\Delta\hat{I} = \sqrt{\eta}\,\alpha_{\mathrm{LO}}^{*}\,(\sqrt{\eta}\,\hat{a} + \sqrt{1-\eta}\,\hat{b}) + \sqrt{\eta}\,\alpha_{\mathrm{LO}}\,(\sqrt{\eta}\,\hat{a}^{\dagger} + \sqrt{1-\eta}\,\hat{b}^{\dagger}) \tag{2.8}$$

with $\hat{b}$ being the mixing of the two vacuum operators $\hat{b} = (\hat{b}_2 - \hat{b}_1)/\sqrt{2}$. Therefore, the losses can be accounted for by mixing the interferometer beams with vacuum inputs on two beamsplitters or even only one, if one puts it into the probe beam before the 50:50 beamsplitter.

## 2.2 Experimental setup

The reason for characterizing and testing the following interferometer setup is the idea to measure the phase of the single photons that are sent through the science chamber of the YQO experiment. With the help of a 2D- and 3D-magneto-optical-trap (MOT), Ytterbium atoms are trapped to form a cloud of ultracold atoms in a science chamber. The MOTs are working on two transistions, one of which is the $6s^2\ {}^1S_0 \rightarrow 6s\ 6p\ {}^1P_1$ transition of $^{174}$Yb with a frequency of $\nu = 751.527$ THz [9]. The same laser driving this transition is used for the measurements in the following homodyne detection setup. One of the atoms in the science chamber is excited to a Rydberg state while the others stay in the ground state due to Rydberg blockade to form a so called Rydberg superatom [10]. When sending photons through this cloud, the state of the superatom, consisting of either the ground state or the excited superatom state including the phase gets mapped on a photon whose quantum state $\cos(\vartheta/2)\,|0\rangle + \sin(\vartheta/2)\,|1\rangle$ can be determined afterwards [5].

The interferometer setup shown in Figure 2.3 consists of a light source that is a 399 nm TA-SHG[1] laser from Toptica. A fraction of this light is guided to the setup through a fiber. To maintain a stable power at the input of the interferometer, the polarization is cleaned by a $\frac{\lambda}{2}$ waveplate and a polarizing beamsplitter (PBS). The waveplate is rotated in a way that the PBS transmits a maximum of the intensity and reflects a minimum. The light transmitted through this PBS, which corresponds to horizontally polarized light, is sent into the interferometer.

After the PBS the light is split into two unequally strong arms by a 1:99 beamsplitter. Due to the terminology used in the YQO experiment, the weaker beam will be referred to as "probe beam" and the stronger one as "local oscillator (LO)". The probe arm is simulating the beam path of the experiment where single photons are sent through the atomic cloud and pick up the state of the Rydberg superatom. To get to this "single-photon" level it is possible to install several neutral density (ND) filters in the probe beam which further reduce the intensity of this beam. By installing acousto-optical modulators (AOM), one in each beam, it is possible to tune the relative phase, intensity and frequency of the two beams. This is helpful for temporarily turning the setup into a heterodyne interferometer for characterizing measurements.

After overlapping the two beams on a second beamsplitter of the splitting ratio 50:50 each output beam is centered on one photodiode of the balanced photodetector (BPD)[2] with the help of spherical mirrors. The detection area of the BPD is hit at the Bragg angle to reduce losses by reflection [7].

[1] tapered amplifier - second harmonic generation
[2] Thorlabs PDB 230A

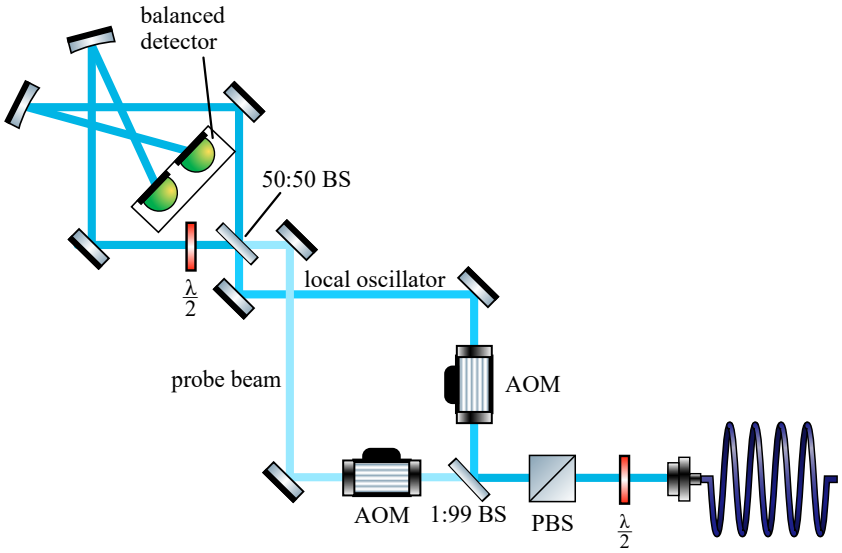


Figure 2.3: The interferometer setup: The laser light is guided to the setup through a fiber. After polarization cleaning with a $\lambda/2$ wave plate and a polarizing beamsplitter the beam is split up into two unequal parts with a 1:99 beamsplitter. Before the two beams are overlapped on a 50:50 beamsplitter, in each beam an acousto-optical-modulator optimized in the $-1$st diffraction order is installed. Adding an additional mirror in the beam path before the second beamsplitter enables to overlap the beams using more degrees of freedom. The two output beams are centered on the two photodiodes included in the balanced photo detector. To ensure a better balancing than possible by only adjusting the beamsplitter by hand, another $\lambda/2$ wave plate is installed in one of the beams.

Nevertheless, a certain amount of the light gets reflected which corresponds to a reduced quantum efficiency of the detector.

The two signals detected on the photodiodes of the balanced photodetector can be observed with an oscilloscope at their respective monitor outputs +/-. Additionally, the difference of these signals is calculated and amplified electronically by the detector and can be observed at a third output, labeled as radiofrequency (RF) output. If the 50:50 beamsplitter is installed in the right angle, both beams are equal in intensity and the RF output will be centered at zero. To make the balancing as good as possible one can adjust the $\lambda/2$ wave plate in one of the output arms in its rotational mount. This balancing assures that the intensity fluctuations of the laser will not display in the RF output and will therefore not contribute to the noise measured. The RF output, which in the following will often be referred to as "difference signal", is filtered with a 15 MHz lowpass filter to already filter out unwanted high-frequency noise before saving the data from the oscilloscope.

CHAPTER 3

# Interferometer stability

In this chapter I present the characterization of the phase stability of the interferometer. To measure the small phase delays that photons undergo as they pass through the cloud of ultracold Ytterbium atoms, the phase of the interferometer itself needs to be very stable. The analysis of the stability can be done in different ways either by using a heterodyne configuration of the setup and extract the phase via Hilbert transform of the measured interference fringes or by homodyning and, after setting the phase to zero, letting the interferometer drift by itself and measuring the phase directly. Drifts in phase can be induced by any external disturbances that change the relative path length of the two interferometer arms. This includes changing the refractive index of the air by temperature changes and air flow as well as mechanical vibrations of the table or the optical elements in the setup.

## 3.1 Phase stability from heterodyne measurements

The setup is intended to measure phases by homodyne detection but the AOMs in the two input arms of the interferometer can be used to artificially induce a difference in frequencies of the two beams. This method of heterodyne interferometry leads to a beating in the interferometer arms which can be observed as interference fringes on an oscilloscope. The drifts in phase of the interferometer can be seen in the measured interference fringes when looking at the zero-crossings of the signal. Analyzing the distances between these zero-crossings can be a way of extracting the drifts of the interferometer phase. In that way, I would be able to extract two data points for each period of the interference signal. To increase the size of the phase data sample that can be extracted from a measurement I chose to use the Hilbert transform to compute an analytic signal from the data and extract the phase fluctuations from that. By this method, phase information can be obtained from every data point of the measurement file. By only checking the zero-crossings I would also not be able to evaluate the phase drifts for very short time intervals because of the comparably long periods and thus distances between zero-crossings except when applying a even higher beating frequency. Without losing transmission efficiency this is only possible to a certain extend because of the frequency range of the AOMs.

### 3.1.1 Phase extraction by the Hilbert transform

The general idea of the Hilbert transform method is to compute an analytic signal, which is a complex number, and calculating the phase from that signal. Real part and imaginary part of this complex

number are the measured signal and its Hilbert transform, respectively. From this analytic signal, we can calculate the absolute value which gives the envelope function of the measured signal. The phase angle is obtained from the argument of the analytic signal.

Following Frederick W. King's *Hilbert transforms* Volume 1 [11] and 2 [12] I give an overview of which properties of the Hilbert transform can be used to process the data.

The Hilbert transform $Hf(x)$ of a signal $f(x)$ is defined as

$$Hf(x) = \frac{1}{\pi}\, p.v. \int_{-\infty}^{+\infty} \frac{f(y)\mathrm{d}y}{x-y}. \tag{3.1}$$

The integral is evaluated with the Cauchy principal value (p.v) since the function is not always integrable. When Hilbert transforming a time domain signal $s(t)$ we can write the integral form of the Hilbert transform as a convolution of the signal $s(t)$ and the kernel function $h(t) = \frac{1}{\pi t}$

$$Hs(t) = s(t) * h(t). \tag{3.2}$$

The Hilbert transform operator is often also called 90° phase shifter. Let us consider a signal that is the sum of different sine functions of different frequency components $k\omega$, phase offsets $\phi_k$ and amplitudes $a_k$

$$s(t) = \sum_{k=1}^{\infty} a_k \sin(k\omega t + \varphi_k), \tag{3.3}$$

then the transformed signal becomes

$$Hs(t) = \sum_{k=1}^{\infty} a_k \sin(k\omega t + \varphi_k - \frac{\pi}{2}). \tag{3.4}$$

Essentially, the signal was shifted by a phase of 90°.

An analytic signal $f(t)$ is a complex function the imaginary part of which is the Hilbert transform of the real part

$$f(t) = g(t) + i\, Hg(t) \tag{3.5}$$

where $g(t)$ is the input signal. Transferring the analytic signal $f(t)$ to the frequency domain, we can see that only the positive frequency components of the signal remain. This can be shown by applying the Fourier transform to Equation 3.5

$$\mathcal{F}f(t) = \mathcal{F}g(t) + i\,\mathcal{F}Hg(t). \tag{3.6}$$

Using the definition in terms of the convolution in Equation 3.2 we obtain

$$\begin{aligned} F(\omega) &= G(\omega) + \operatorname{sgn}\omega\, \mathcal{F}Hg(t) \\ &= G(\omega)(1 + \operatorname{sgn}\omega) \end{aligned} \tag{3.7}$$

with $\mathcal{F}h(t) = -i \operatorname{sgn}\omega$ and $\operatorname{sgn}(\omega)$ the signum function

$$\operatorname{sgn}(\omega) = \begin{cases} -1, & \omega < 0 \\ 1, & \omega > 0 \end{cases}. \tag{3.8}$$

This results in

$$F(\omega) = \begin{cases} 0, & \omega < 0 \\ 2G(\omega), & \omega > 0 \end{cases}. \tag{3.9}$$

Having transformed the signal data into an analytic signal, an envelope function of the data can be calculated by taking the absolute value of the analytic signal. The phase is extracted by the angle of this complex number.

### 3.1.2 Implementing the Hilbert transform

To test the implementation of the Hilbert transform[1], I create an artificial signal $s(t) = \sin\omega t$ with a frequency $\omega = 10\,\mathrm{Hz}$. The function calculates the analytic signal and from that the absolute value and therefore envelope of every datapoint. If the implementation works flawlessly, the envelope of a time interval that is an integer multiple of the period should be a flat line. We can see that this is the case in the upper plot of Figure 3.1. For every data point also the phase can be extracted by calculat-

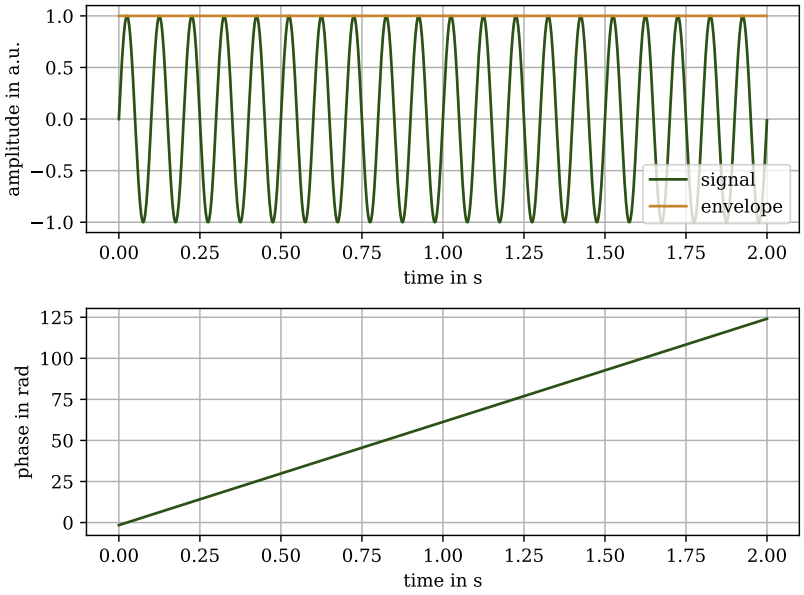


Figure 3.1: Exemplary Hilbert transform plots of a sinusoidal function. In the upper plot the measured signal and its envelope are shown, whereas the lower plot shows the unwrapped phase of the signal.

ing the angle in the complex plane. The lower plot in Figure 3.1 shows the unwrapped phase, which

[1] I used the `python` module *scipy.signal.hilbert*.

means that the phase angle is not limited to the interval $[0, 2\pi]$ but adds up with every full phase oscillation.

A signal measured in the heterodyne interferometer will display fluctuations of the phase and amplitude caused by characteristics of the setup due to it not being completely shielded from external impacts. An exemplary measurement of the interference signal in the heterodyne configuration using a beating frequency of 100 kHz is shown in Figure 3.2. Using the difference signal for the evaluation helps to suppress technical noise, but there are still fluctuations in amplitude which cause the envelope function to not exactly be a flat line. In fact, we can observe deviations from a flat envelope. Additionally, a mismatch of the signal amplitudes at the beginning and end of the data sample can lead to artefacts at the edges of the data. Inherent phase drifts of the interferometer can be extracted from the data by

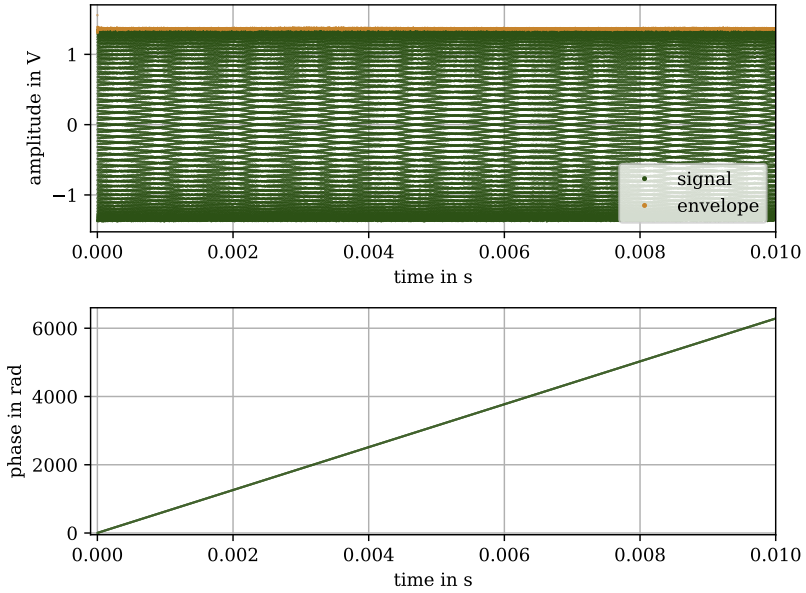


Figure 3.2: Exemplary Hilbert transform plots of real data measured with a beating frequency of 100 kHz. The upper plot shows the measured signal on the oscilloscope as well as the envelope obtained from the Hilbert transform. Below that, the unwrapped phase of the beating oscillation is plotted.

comparing the measured phase to the expected phase of a perfect beating signal, corresponding to a linearly increasing phase. The lower plot in Figure 3.2 shows the phase extracted from the measured signal through the Hilbert transform method after unwrapping. Doing a linear fit on the unwrapped phase of the measured data and subtracting the fit line corresponds to subtracting the phase that cumulates from the beating from the measured phase drifts. One is left with only the small deviations of the phase that stem from phase noise. Figure 3.3 displays these remaining fluctuations. The artefact of a few data points being at a much lower value at $t = 0\,\mathrm{s}$ appears because of the mismatch of the signal amplitude of the first and last point. This same artefact can be found at the last entries in the data sample. To avoid those artefacts in the evaluation of the data it is possible to cut the first and last values out of the sample after the transform is done. The remaining data will be sufficient for further uses, for example computing an Allan deviation as described in subsection 3.2.1.

The subtracted phase plotted in Figure 3.3 shows a small oscillation on short timescales which is why I zoomed into it further in Figure 3.4. From this zoomed-in picture we can find the oscillation to be of a frequency of around 1 kHz from which follows that it is not a residual of the beating frequency caused by the Hilbert transform not working optimally. As I show in subsection 3.2.3, this oscillation is in fact not related to the beating frequency but to acousto-mechanically coupled technical phase noise of the interferometer.

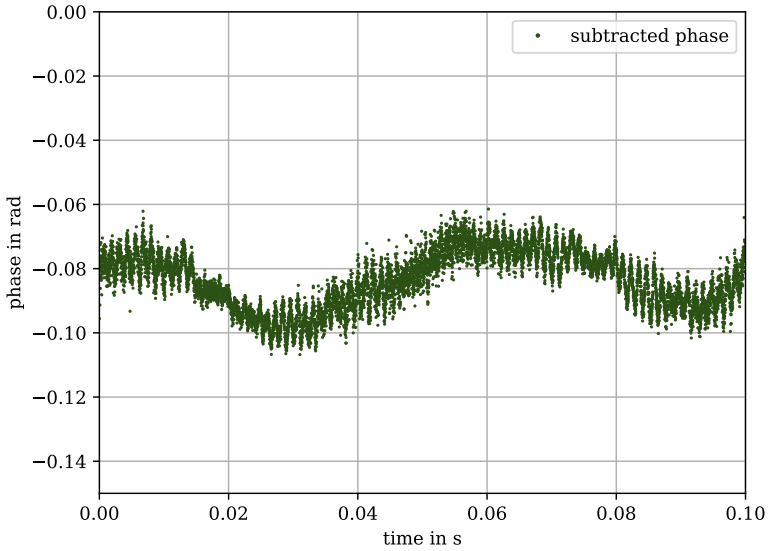


Figure 3.3: Exemplary plot of the subtracted phase of measured data at a beating of 100 kHz. An additional oscillation is visible.

## 3.2 Stabilizing the interferometer

In order to stabilize the interferometer, I aim to quantify the phase noise of the setup on different timescales. The Ytterbium experiment will consist of several light pulses of 1-10 µs over the time interval of 10 ms. On this timescale, the phase stability should be at the best possible value. The following section will discuss the Allan deviation as a tool to characterize the inherent stability of the interferometer as well as adjustments of the setup to optimize the stability.

### 3.2.1 Calculating the Allan deviation

As mentioned above, I use the Allan deviation for the characterization of the phase stability of the interferometer setup. The Allan deviation $\sigma_y$ is a measure on how big the fluctuations of an observed variable are on different timescales. The general approach is to divide the data into time intervals $\tau$ and average the variable in this time interval. Taking all the time intervals of the same length into account, the fluctuation between the intervals on this specific timescale is derived. The set of data points that is produced by doing this for several different time intervals typically displays a certain

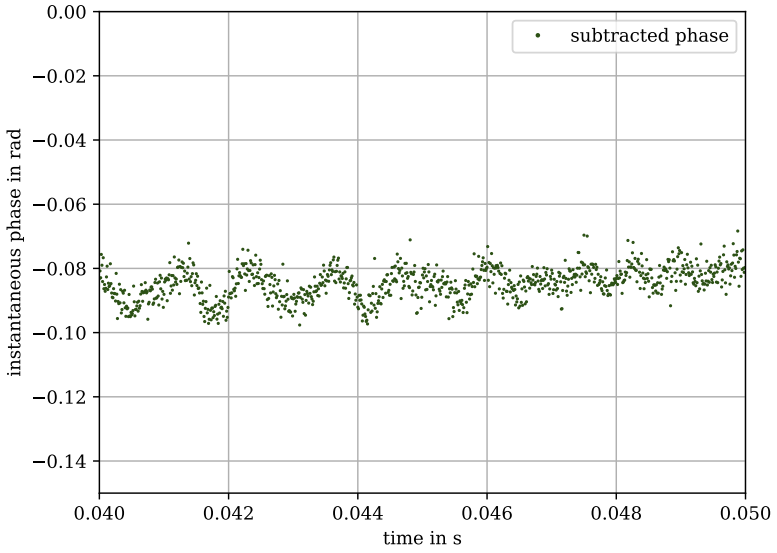


Figure 3.4: Exemplary plot of the subtracted phase of measured data at a beating of 100 kHz. Zooming into the time axis shows the additional oscillation to be on a scale of 1 kHz.

feature. For very small averaging times $\tau$, the Allan deviation is comparably high because every interval contains vastly different values. Averaging over slightly longer times leads to a decrease of $\sigma_y$ as very fast fluctuations average out. When the length of $\tau$ reaches a certain point, the Allan deviation increases again due to long scale drifts that are only visible when looking at longer sections of the data.

To improve the certainty of the Allan deviation one can use the overlapping Allan deviation. It consists in not only using the number of time intervals $k$ that fit into the measurement time $T$ as $k = T/\tau$ where one interval begins at the time the last one ends but instead overlaps those time intervals by having them start at all sample points in timesteps of $\tau_0$. Following this scheme the deviation can be calculated for a greater number of time intervals and therefore reduce the uncertainties. The `python` implementation *allantools* [13] directly computes the Allan variances $\sigma_y^2(m\tau_0)$ for an array of different $\tau$ as

$$\sigma_y^2(m\tau_0) = \frac{1}{2(m\tau_0)^2(N-2m)} \sum_{n=1}^{N-2m} (x_{n+2m} - 2x_{n+1m} + x_n)^2, \tag{3.10}$$

where $\tau = m\tau_0,\ m \in \mathbf{N}$ with the inverse sampling rate $\tau_0$. $n$ denotes the summation index going from 1 to $N - 2m$ where $N$ is the number of the measured sampling points $x_n$. The Allan deviation $\sigma_y$ is obtained by taking the square root of the variance and can be plotted against $\tau$.

Making use of the Allan deviation to quantify phase fluctuations on the measured data requires a sample of phase data. This phase data is obtained from applying the Hilbert transform to the measurements in the heterodyne configuration as described in subsection 3.1.2. To not distort the deviation

on certain timescales, the edges of the data sample where the artefacts from a mismatch of the signal amplitudes would lead to a much larger phase deviation are cropped out.

### 3.2.2 Air currents on the table

To measure the phase and compute the Allan deviation for the following measurements, I set the difference frequency of the two AOMs to 100 kHz. That way, for a measurement of the difference signal with a sampling rate of 10 MS/s and a duration of 1 s I can analyze the Allan deviation for a regime that includes both the pulse duration as well as the complete time of the experiment sequence. From the saved difference signal of these measurements I extract the phase by using the Hilbert transform explained in subsection 3.1.2. Figure 3.5 shows the Allan deviation of the measurements performed with the setup standing on the table freely (without enclosure). As an attempt to lower the phase drifts mainly in the regime of hundreds of milliseconds I built an enclosure to shield the setup from air currents that come from the temperature stabilizing flow box on the table. The effect on the Allan deviation is shown in the comparing plot in Figure 3.5. Especially on the larger timescales, the phase drifts reduced up until a factor of 3. Improving the stability of the phase on timescales of hundreds of milliseconds leads to a local maximum becoming more visible in the regime between $10^{-3}$s and $10^{-4}$s. Since this is not a characteristic of an ideal Allan deviation, it will be investigated further to possibly be reduced.

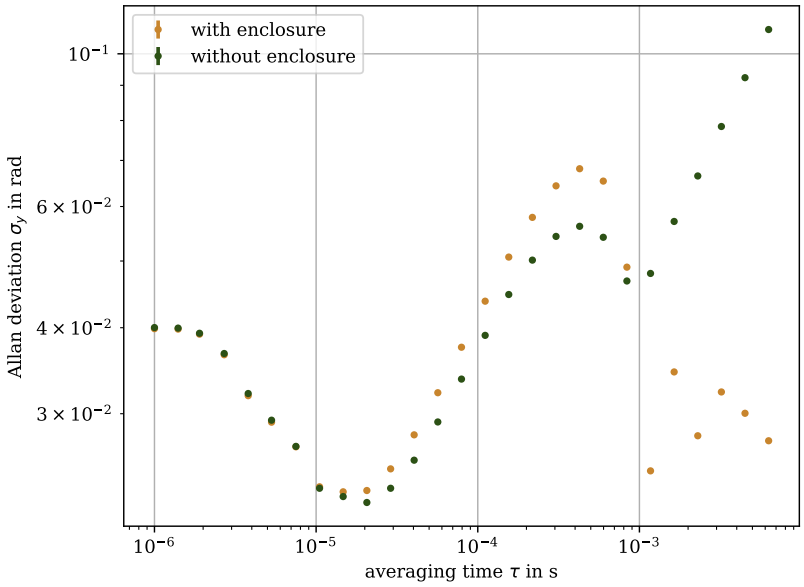


Figure 3.5: Comparison of the Allan deviation from heterodyne measurements with a beating frequency of 100 kHz with and without the enclosure to shield the setup from air currents.

### 3.2.3 Mechanical resonances

The subtracted phase of the interferometer showed an additional oscillation on the order of 1 kHz. To exclude this being a residual from the beating frequency or being influenced by it, I checked the phase data for another beating frequency. In fact, for a beating frequency of 1 MHz, the same phase noise is

visible. This is shown in Figure 3.6. Counting roughly 8 oscillations in this time frame of 10 ms this

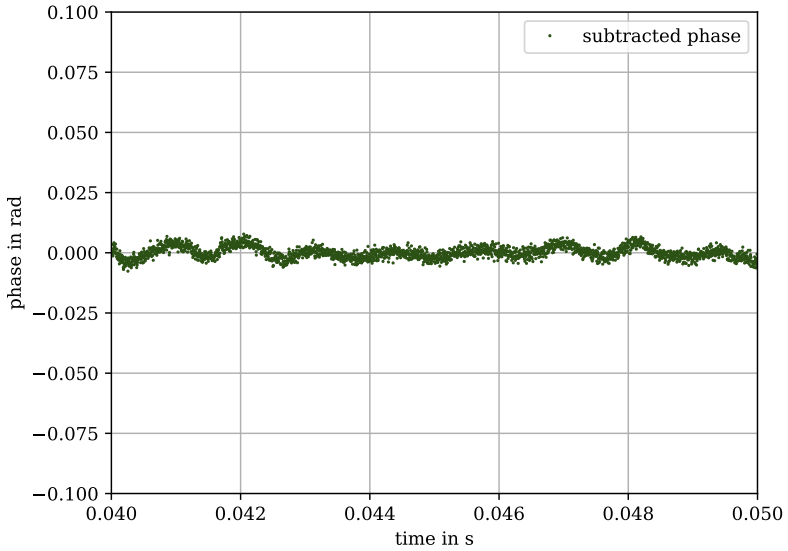


Figure 3.6: Subtracted phase of the 1 MHz beating measurement with a visible 1 kHz oscillation.

corresponds to the peak in the Allan deviation for time intervals $\tau$ between $10^{-3}$ s and $10^{-4}$ s. To find out what exactly causes this disturbance, I intentionally disturbed the setup acoustically and mechanically to reproduce the oscillation on the given timescale. By knocking on the table, stomping or loud noises the oscillation could even be seen on the oscilloscope signal. With the help of the oscilloscope signal, I could specify the oscillation to a frequency of 850 Hz. With that knowledge it was possible to artificially disturb the interferometer on its resonance frequency by applying a soundwave of this frequency[2]. Holding the sound source to different elements in the setup, one could see the amplitude of the extra oscillation increase significantly. I concluded that some of the optical elements or their mounts must have a resonance at 850 Hz with a high quality factor. I could locate the element with the largest influence by damping all the mounts one after another with my finger. To possibly remove the additional oscillation I replaced the specific mirror mount that had a high impact on the phase stability and performed a new stability measurement. As can be seen in Figure 3.7, the local maximum could in fact be reduced by replacing the most resonating mirrormount but is still very prominent. It was already visible in the time-domain signal on the oscilloscope that the additional oscillation was reduced by damping this specific mirror mount but did not completely vanish due to other elements exhibiting lower quality factor resonances. This is why the Allan deviation still shows the local maximum and not the standard feature of just having one minimum. The absolute values of the Allan deviation are limited by the maximal value of $(0.0678 \pm 0.0002)$rad which corresponds to $(3.88 \pm 0.02)°$. From this follows that during the time of the experimental sequence, the setup will drift at most 3.88° by itself. For even lower drifts, one has to shield the interferometer even better from any acoustic or mechanical influences.

[2] This frequency corresponds to a note pitched between $Ab_5$ and $A_5$.

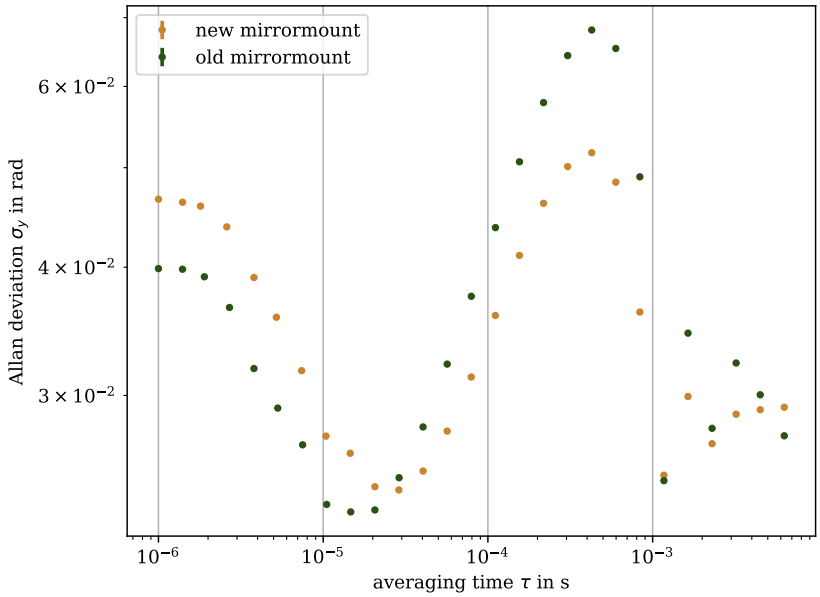


Figure 3.7: Comparison of the Allan deviation measured at 100 kHz before and after changing a particularly resonant mirror mount.

## 3.3 Homodyne measurements

The purpose of the interferometer is homodyne detection and we have to consider that the stability in the homodyne configuration might differ from the one measured with a beating frequency. To compare the stability of both methods, the two AOMs are set to the same frequency. The difference output of the photodetector is used to observe the phase drifts between the two interferometer arms.

Letting the interferometer drift by itself, one loses the reference of the beating signal. This is why, before taking the data, the relative phase needs to be set to zero. This can be done with one AOM by changing the phase such that the difference signal on the oscilloscope is centered around zero. In contrast to the heterodyne method, the taken data does not have to undergo the Hilbert transform but can directly be used for calculating the Allan deviation. Because the relative phase is set to zero, we can approach small deviations from zero as the linear part of an interference fringe, since

$$\sin x \approx x \text{ for } x \to 0, \tag{3.11}$$

and obtain the absolute phase by dividing the measured values by the amplitude of the difference signal measured with a beating frequency. In Figure 3.8, one can see the comparison between homo- and heterodyne measurements. For short time intervals, the homodyne method shows a better stability whereas in the regime of interest the to methods show very similar stabilities. The difference at $\tau$ on the order of $10^{-6}$ to $10^{-5}$ could be induced by the beating. It is possible that the Hilbert transform is influenced by small deviations in amplitude and thus exhibits additional phase noise on the order of the used beating frequency. This comparison shows that, similar to as it was the case for the heterodyne method, the phase is stable with a fluctuation of a maximum of $(0.0738 \pm 0.0004)$ rad corresponding to $(4.23 \pm 0.03)°$.

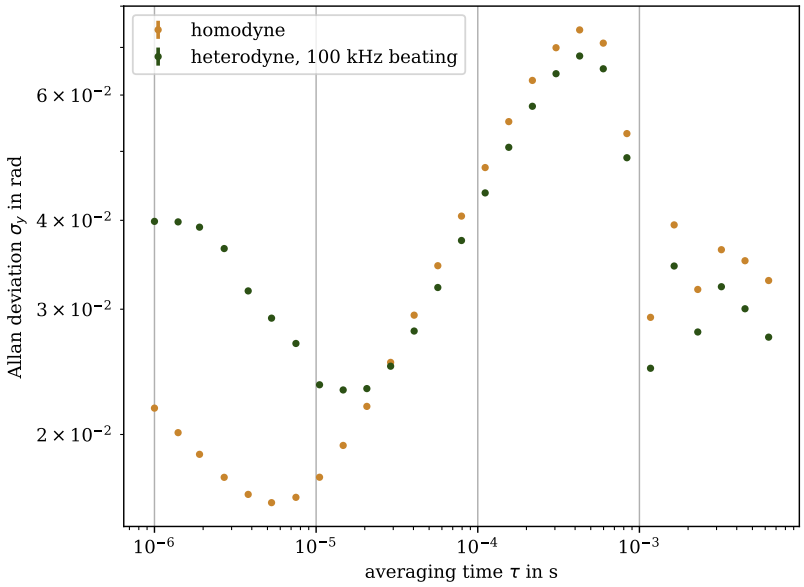


Figure 3.8: Comparison of the Allan deviation of homo- and heterodyne measurements.

Measuring the phase of the interacting photons with a certainty of 4° is a tremendous improvement compared to not being able to obtain any phase information. To not be limited by the local maximum of the Allan deviation when performing phase measurements on single photons in the experiment, in the future it is possible to investigate the issue of mechanical resonances in the setup further, if necessary. Working on this thesis, I did not only look into the phase stability but also into the ability to observe a signal when measuring in the few-photon regime of the probe beam. No matter how stable the phase of the interferometer is, if one is not able to identify the interference signal and thus the phase of the detected photons, no new information on the quantum state of the photons is obtained. For this reason, I did another set of measurements with a beating frequency to compare the signal level to the one of the noise.

CHAPTER 4

# Few-photon interferometer

In the YQO experiment, the probe beam is sending only a few photons through the science chamber with every pulse which is several microseconds long. For that reason, we need to know if a signal would still be visible for probe powers corresponding to this photon rate. By attenuating a source of coherent light with ND filters we achieve photon rates close to the requirements of the experiment. In this chapter, calculations on the visibility of the interference signal in the heterodyne configuration and the signal-to-noise ratio for decreasing probe powers are executed as well as the evaluation of the noise of the taken data.

## 4.1 Visibility of the interference signal

When taking a measurement it is important to always tune the setup to the maximal visibility $V$ reachable so that data from a measurement where a specific condition was varied is still comparable concerning the measured amplitudes and voltage levels. The visibility, also called interference contrast, is defined as

$$V = \frac{I_{\max} - I_{\min}}{I_{\max} + I_{\min}}, \tag{4.1}$$

where $I_{\max}$ is the intensity of the interference signal at constructive interference and $I_{\min}$ is the intensity of the interference signal at destructive interference. For the case of a 50:50 splitting between probe and local oscillator, destructive interference will lead to $I_{\min} = 0$ and thus to a visibility of 100%. Splitting the two beams at a ratio of 1:99 or attenuating the probe beam even further one needs to calculate the maximal and minimal intensities because the destructive interference will not result in exact cancelling of the two beams. To visualize the interference signal and the mentioned intensity values we can have a look at Figure 4.1.

In Quantum Optics we can describe the electric field $\vec{E}(\vec{r}, t)$

$$\vec{E}(\vec{r}, t) = E_0 e^{i(\vec{k}\vec{r} + \omega t + \varphi)} \tag{4.2}$$

depending on the time $t$ and position vector $\vec{r}$ as a wave with the amplitude $E_0$, the wave vector $\vec{k}$ and a phase $\varphi$ oscillating with the frequency $\omega$. To calculate the visibility according to P. Meystre and M. Sargent III.'s *Elements of Quantum Optics* [14] we decompose the electric field $\vec{E}(\vec{r}, t)$ into positive and

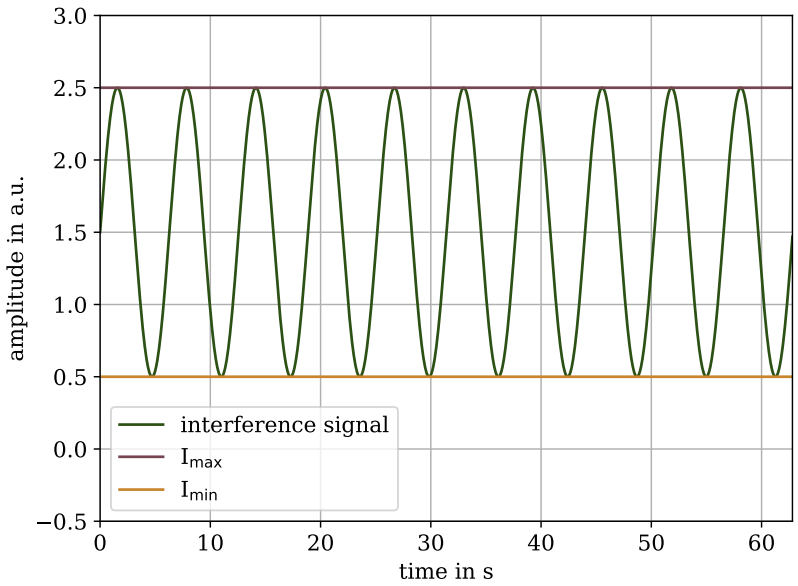


Figure 4.1: An artificial interference signal $s(t) = \sin(t) + 1.5$ with a visibility $< 1$ providing the minimal and maximal intensity values to calculate the visibility.

negative frequency components

$$\vec{E}(\vec{r},t) = \vec{E}^{+}(\vec{r},t) + \vec{E}^{-}(\vec{r},t), \tag{4.3}$$

where

$$\vec{E}^{-}(\vec{r},t) = |\vec{E}^{+}(\vec{r},t)|^{*} \tag{4.4}$$

holds. For the further considerations we only take the positive component $\vec{E}^{+}(\vec{r},t)$ into account [14]. The interfering electric fields now have to be added up due to their respective path lengths $\vec{r}_{1,2}$ and travel times $t_{1,2}$

$$\vec{E}^{+}(\vec{r},t) = \vec{E}^{+}(\vec{r_1},t_1) + \vec{E}^{+}(\vec{r_2},t_2). \tag{4.5}$$

The intensity of the interference signal $I$ is proportional to the absolute square of the electric field

$$\begin{aligned} |\vec{E}^{+}(\vec{r},t)|^2 &= |\vec{E}^{+}(\vec{r_1},t_1)|^2 + |\vec{E}^{+}(\vec{r_2},t_2)|^2 + 2\,\mathrm{Re}(|\vec{E}^{+*}(\vec{r_1},t_1)\vec{E}^{+}(\vec{r_2},t_2)|) \\ &= |\vec{E}^{+}(\vec{r_1},t_1)|^2 + |\vec{E}^{+}(\vec{r_2},t_2)|^2 + 2\,|\vec{E}^{+}(\vec{r_1},t_1)|\,|\vec{E}^{+}(\vec{r_2},t_2)|\cos\varphi \\ \Rightarrow I &\propto I_1 + I_2 + 2\sqrt{I_1 I_2}\cos\varphi \end{aligned} \tag{4.6}$$

For the cross term we additionally have to consider the phase angle $\varphi$ between the two fields. Since the cosine only takes values between -1 and 1, the intensity on the detectors will have its maximum and minimum for

$$I_{\mathrm{max/min}} \propto I_1 + I_2 \pm 2\sqrt{I_1 I_2}. \tag{4.7}$$

When calculating the visibility, the prefactors cancel out and are not necessary to calculate.

With the help of this formula, the expected contrast can be calculated for every probe power I

am measuring. Thus, it is possible to maximize the contrast for every attenuation measurement which is required because the ND filters can bring in a slight misalignment of the beam pointing.

## 4.2 Characterization of ND filters

Measuring a strongly attenuated beam on the few-photon level can be challenging due to background noise and the detection limit of the powermeter. To reliably measure the attenuation of the ND filters I use the strong LO beam. In that way I am able to measure the intensities before and behind the filter with a powermeter to then calculate the actual transmission of every filter shown in Table 4.1. When attenuating the the probe beam with these filters, only the intensity without any attenuation has to be measured, all further intensities can be calculated afterwards.

Table 4.1: Optical densities and transmission of the used ND filters

| OD | Expected transmission / % | Measured transmission / % |
|---|---|---|
| 0.1 | 79.4 | 87.41 ± 0.02 |
| 0.2 | 63.1 | 70.35 ± 0.02 |
| 0.3 | 50.1 | 58.05 ± 0.02 |
| 0.4 | 39.8 | 41.92 ± 0.02 |
| 0.5 | 31.6 | 32.23 ± 0.02 |
| 0.6 | 25.1 | 25.62 ± 0.02 |
| 1 | 10.0 | 9.07 ± 0.02 |
| 2 | 1.0 | 0.28 ± 0.02 |
| 3 | 0.1 | 0.015 ± 0.013 |
| 4 | 0.01 | 0.002 ± 0.013 |

## 4.3 Signal-to-noise ratio

The key of the interferometer is to have a signal which is much larger than any kind of noise on this signal. To characterize the ability to see the signal above the noise I calculate the signal-to-noise ratio (SNR). This is done by setting the AOMs to a difference in frequencies and observing the sinusoidal beating signal at the difference output of the photodetector. The value for the SNR is calculated to

$$\mathrm{SNR} = \frac{U_{\mathrm{amplitude}}}{U_{\mathrm{RMS}}}, \tag{4.8}$$

where $U_{\mathrm{amplitude}}$ is the amplitude of the interference signal measured on the oscilloscope in Volt and $U_{\mathrm{RMS}}$ is the root mean square (RMS) of the noise. This noise on the signal is computed by fitting a sine to the taken data as shown in Figure 4.2 and then subtracting this ideal sine from the data points. The residual noise is presented in Figure 4.3. To be able to extract the signal from the measurement we want the signal-to-noise ratio to not get smaller than 1 which is where the RMS of the noise has the same value as the amplitude of the signal. Below that, the interference is not distinguishable from the noise anymore.

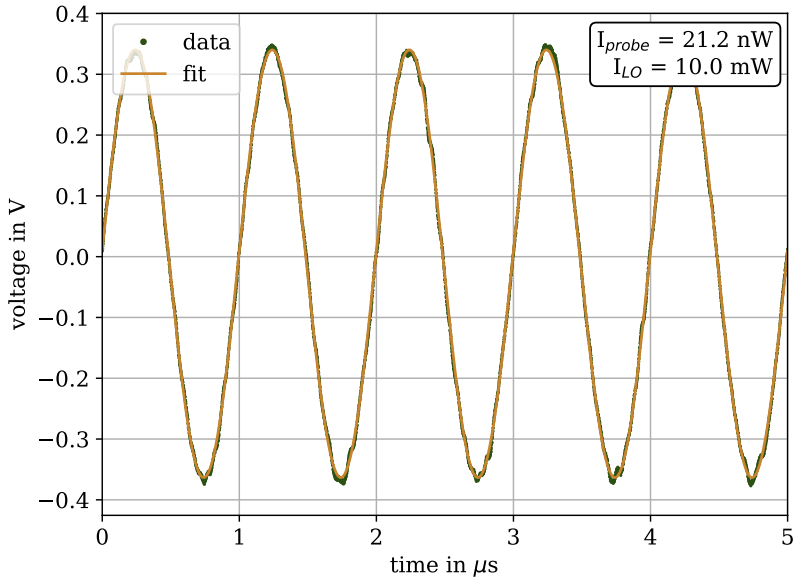


Figure 4.2: Exemplary plot for the fitted sinusoidal signal already attenuated to a probe power of 21.2 nW

## 4.4 Entering the few-photon regime

To approach the desired few-photon regime I attenuate the probe beam with the ND filters characterized in Table 4.1. Using the heterodyne configuration (see section 3.1), reducing the probe power leads to reduction of the amplitude of the interference signal until it eventually vanishes in its own noise. In the following section I aim to characterize and improve the detection sensitivity of the homodyne detector.

### 4.4.1 Noise on the local oscillator beam

In the best case, all of the remaining noise after subtracting a sinusoidal fit from the interference signal stems from the shot-noise of the LO beam. In the case of balanced homodyne detection, the signal should not exhibit any classical noise caused by e.g. intensity fluctuations because those are cancelled out by measuring at the differential output of the photodetector. At an almost perfect balancing, the detector should operate at the shot noise limit [15]. Shot noise classifies as quantum noise and arises from quantum fluctuations of the electric field [16], so it is not suppressed by the balanced detection. To verify that indeed, all the noise on the signal is the LO shot noise, I measure the pure noise of the LO beam by completely blocking the probe beam. This signal and its root mean square value are shown in Figure 4.4. If the RMS for the measurement of the pure LO noise is at the same value as the RMS of the noise after subtracting the sine from the interference signal we can conclude that all the noise on the measured signal is coming from the local oscillator.

One can see that for probe powers on the scale of μW the root mean square of the residual noise is significantly higher than the pure noise of the LO beam. This is the case both for the LO power of 1 mW where the noise level is $U_{\mathrm{RMS}}$ = 2.1 mV (see Table 4.2) and for the LO power of 10 mW with $U_{\mathrm{RMS}}$ = 6.1 mV (see Table 4.3) for the pure LO noise. The intensity of the probe beam is high enough

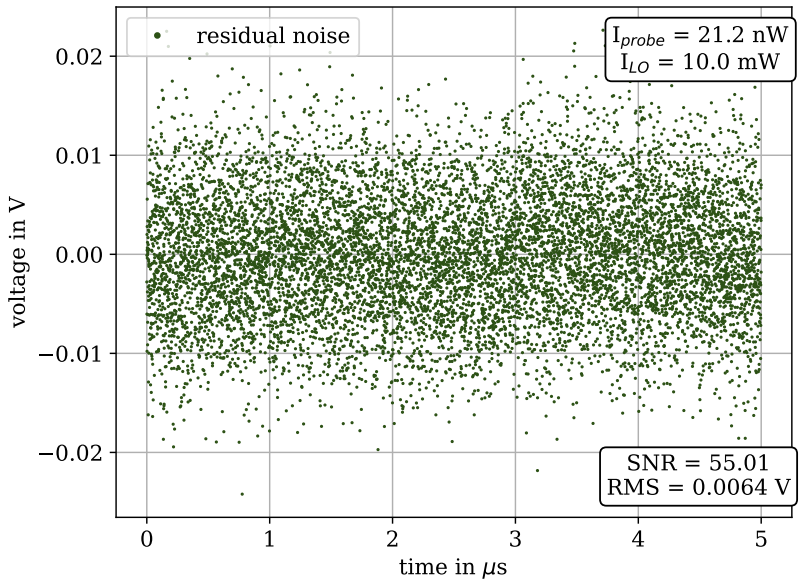


Figure 4.3: Exemplary plot for the residual noise after subtracting the sine at a probe power of 21.2 nW

Table 4.2: RMS values for $I_{\mathrm{LO}}$ = 1 mW at a beating frequency of 1 MHz

| probe power | RMS / mV |
|---|---|
| 8.3 µW | 9.159094(11) |
| 0.75 µW | 10.407567(11) |
| 23.2 nW | 2.148768(11) |
| 2.1 nW | 2.143181(15) |
| 1.2 nW | 2.152224(27) |
| 0.11 nW | 2.151541(97) |
| 3.5 pW | 2.1382(31) |
| 0.31 pW | 2.143(72) |
| 0.04 pW | 2.1(10) |

to add its own shot noise to the one of the local oscillator. This shot noise strongly reduces for lowering the probe power which means that at higher attenuations, the noise on the probe beam is small enough to have no influence on the measured shot noise. For probe powers in the nW and pW regime, the residual noise stabilizes at the noise level of the local oscillator. At a LO power of 1 mW, the residual noise is very stable at the RMS level of 2.1 mV, while for the 10 mW case the noise RMS values are fluctuating around 6.1 mV. In general we can conclude that when approaching the few-photon regime by reducing the probe power, the only significant noise comes from the local oscillator beam.

Comparing the two RMS values for the pure LO noise, one can see that the ratio $R$ between them is

$$R = \frac{0.0061\,\mathrm{V}}{0.0021\,\mathrm{V}} \approx 2.9. \tag{4.9}$$

Table 4.3: RMS values for $I_{\mathrm{LO}} = 10\,\mathrm{mW}$ at a beating frequency of 1 MHz

| probe power | RMS / mV |
|---|---|
| 0.24 µW | 8.272035(11) |
| 21.2 nW | 6.395681(11) |
| 12.6 nW | 6.073368(11) |
| 1.1 nW | 5.972785(11) |
| 35.3 pW | 5.987860(30) |
| 4.5 pW | 6.31443(15) |
| 0.40 pW | 6.0780(19) |
| 0.02 pW | 6.1(21) |

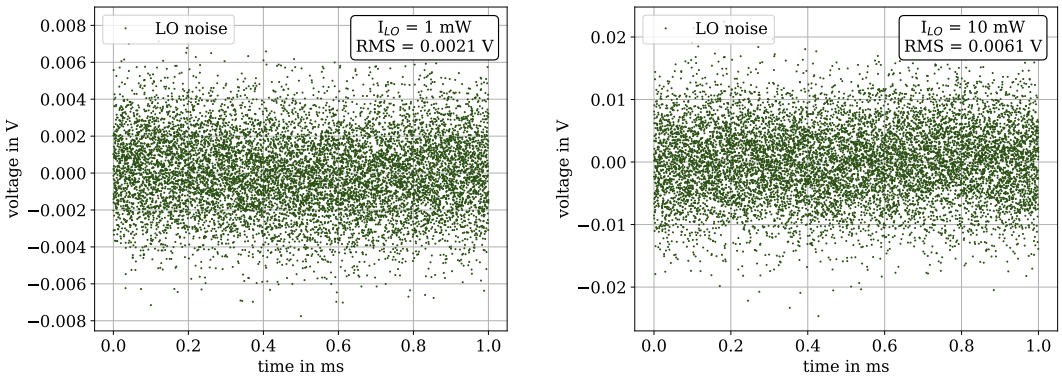


(a) LO power 1 mW

(b) LO power 10 mW

Figure 4.4: Noise of the local oscillator at different beam powers.

If the local oscillator is limited by shot-noise, the ratio in Equation 4.9 is expected to be given by the square root of the ratio between the different beam powers [6]. Equation 4.9 shows the result to be slightly lower than the expectation of $\sqrt{10}$. Therefore, either the local oscillator with a power of 10 mW exhibits noise below the shot noise limit, which is only possible for amplitude squeezed light when the noise level is below that of zero-point fluctuations [17], or the local oscillator with a power of 1 mW exhibits noise above the shot-noise.

### 4.4.2 Noise calculation with a beating frequency

Looking further into the signal-to-noise ratio can provide insight into whether the interferometer signal for different LO intensities reaches the shot-noise limit or not. Acquiring 1 ms of the detector difference signal provides a sufficient number of interference fringes to reliably fit a sine curve, even at strong attenuations, and thus low amplitudes, and evaluate the signal-to-noise ratio derived in section 4.3 for different probe powers.

Figure 4.5 shows the relation between the probe power, expressed as the number of photons $N_\gamma$ per µs, and the signal-to-noise ratio. To calculate the number of photons per second of the probe beam, we recall from section 2.2 that the wavelength of the laser light is 399 nm, which corresponds to

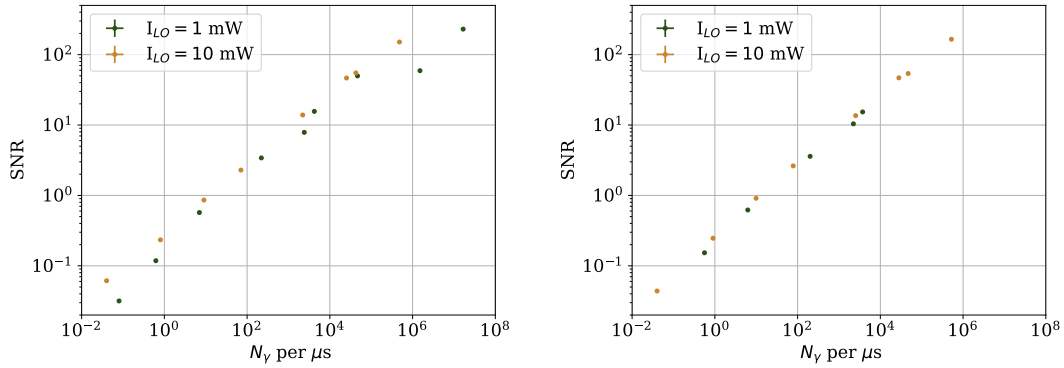


(a) Beating frequency 1 MHz

(b) Beating frequency 100 kHz

Figure 4.5: Signal-to-noise ratio plotted for different LO powers and beating frequencies

$\nu$ = 751.527 THz. The probe beam power $P$ is given as the energy $E$ per time $t$

$$P = \frac{E}{t}, \tag{4.10}$$

and the energy as

$$E = N_\gamma \cdot E_\gamma \tag{4.11}$$

with photon number $N_\gamma$ and photon energy $E_\gamma = h\nu$ where $h$ is Planck's constant. Solving the equations above for $N_\gamma$ we obtain

$$N_\gamma = \frac{P \cdot t}{h \cdot \nu} \tag{4.12}$$

for the photon number. In the case of the LO being shot noise limited, increasing the power will not increase the signal-to-noise ratio. This is due to the fact that while the amplitude of the interference signal will increase with the square root of the ratio between different beam powers, also the shot noise increases by this same factor. Calculating the SNR with Equation 4.8 leads to the cancelling of those two factors. Due to the fact that the ratio between the noise levels does not quite reach the expected value of $\sqrt{10}$ (cf. subsection 4.4.1), there is still a difference visible in the plots. In particular, for the 1 MHz beating frequency setting shown in Figure 4.5, the 10 mW power case shows a more linear increase than the case of 1 mW local oscillator power. It can be concluded that for low local oscillator powers, we are limited by technical noise above the shot noise, but at higher powers which are reasonably high and possible to reach, the technical noise loses its impact and we are purely limited by shot noise.

### 4.4.3 Comparison of measurements in the time- and frequency-domain

When lowering the intensity of the probe beam, the amplitude of the interference signal decreases and disturbances in the interference fringes obtained from the oscilloscope become visible on the signal. A method to extract which additional frequencies are present is to measure the difference signal with a spectrum analyzer. We obtain a spectrum with every frequency component of the interference signal.

In Figure 4.6(a) we can see that in the time-domain the amplitude of the interference signal for

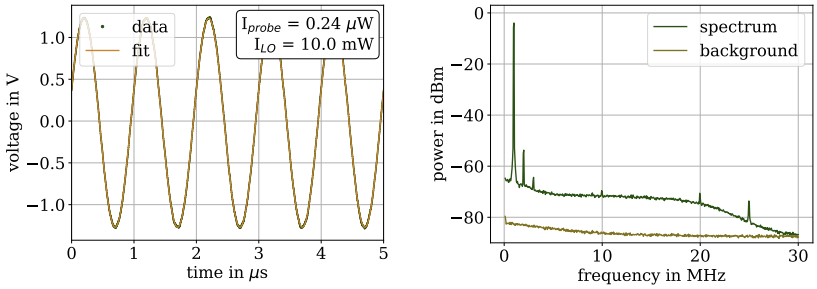


(a) Probe power 0.24 µW

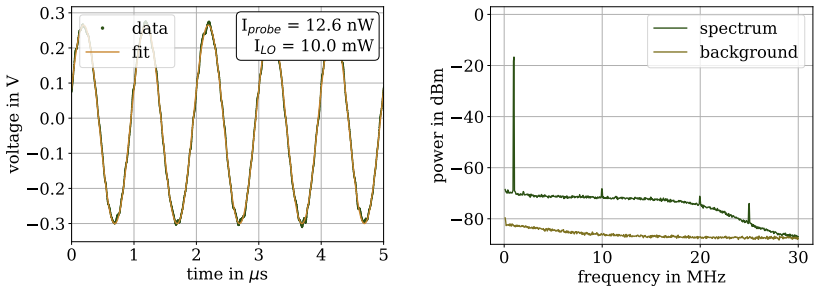


(b) Probe power 12.6 nW

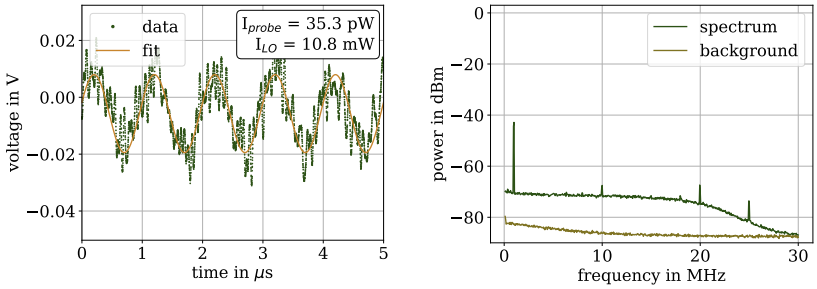


(c) Probe power 35.3 pW

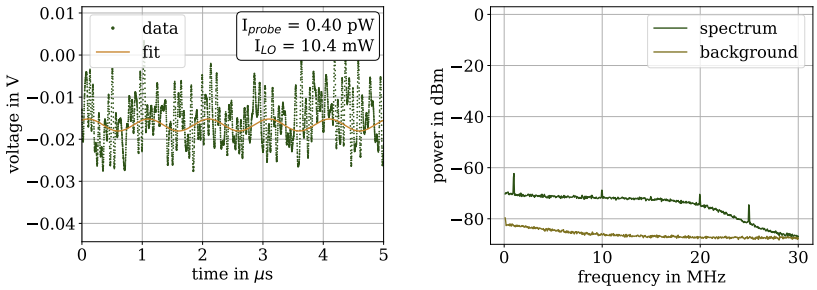


(d) Probe power 0.40 pW

Figure 4.6: Measured interference signals in the time-domain (left) and frequency-domain (right) for different probe powers. With decreasing probe powers, oscillation frequencies other than the 1 MHz beating frequency become prominent in the time domain. In all frequency spectra, the level of the signal for higher frequencies lowers because of the used low-pass filter with 15 MHz cut-off frequency.

higher probe powers is high and the oscillation seems to be of just one frequency, while in the frequency-domain different additional frequencies are visible. Comparing the heights of the visible peaks on the logarithmic scale, it becomes clear that those additional frequency components are negligible in regard to the signal amplitude. The frequencies that are most prominent here are the harmonics of the beating frequency, mostly at 2 MHz and 3 MHz and also frequencies of 10, 20 and 25 MHz. Decreasing the probe power (see Figure 4.6) should lead to the harmonics becoming irrelevant as they are dampened to a very low level. At the same time the higher frequencies, which don't depend on the power of the probe beam and thus stay at the same level, also become visible in the time-domain observations.

At a probe power of $I_{probe} = 12.6\,nW$, shown in Figure 4.6(b), the additional frequencies are still of an amplitude only a fraction of the signal amplitude but the minima and maxima of the time-domain signal already exhibit small fluctuations which get very prominent in Figure 4.6(c) at $I_{probe} = 35.3\,pW$. In the corresponding two spectra it also becomes clear that the amplitude of the 25 MHz oscillation is filtered out by the low-pass filter such that it lies below the level of the general noise and will therefore not be visible in the time-domain. Still, the mixing of the 10 MHz and 20 MHz into the 1 MHz beating is apparent.

Proceeding to an even weaker probe beam of $I_{probe} = 0.4\,pW$, the amplitudes of the actual signal and those of disturbing frequencies become comparable and the signal in the time-domain is not visible anymore. The presented time-domain plots are only a part of the measured data taken in a time frame of 1 ms. Thus, over as many as 1000 oscillations, the fit will find the periodicity of the wanted 1 MHz frequency such that it is possible to fit a sinusoidal function to the data points. As we have seen in subsection 4.4.2, it is possible to calculate the signal-to-noise ratio, but it will be of a value $< 1$ because of the dominant noise.

From the signal-to-noise ratio measurements I can conclude that this setup is suitable for detecting phase shifts in the regime of a few photons per µs. While the SNR values are similar whether a 1 mW or 10 mW local oscillator is used, it is important to always overcome the technical noise and be limited in shot noise, which is the case for the 10 mW LO beam power. One approach to further improve the SNR would be to find and eliminate the sources of the 10 and 20 MHz frequencies. One possible source could be the laser itself. The Pound-Drever-Hall modulation frequency for the used laser is specified to be below 25 MHz. It is possible that the 10 MHz peak comes directly from this modulation while the 20 MHz peak one of the harmonics. In this case it is difficult to eliminate the frequency components. Using a low-pass filter at a lower frequency, e.g. 10 MHz or even lower, could help but could also lead to partly filtering out the information we want to measure.

Being able to measure a signal with a probe beam of only several photons per µs leads the way to perform balanced homodyne detection in the YQO experiment. Measuring the phase of the probe photons that are sent through the cloud of ultracold atoms for scanning the phase angle of the local oscillator for one period makes it possible to reconstruct the quantum states of the photons.

CHAPTER 5

# Conclusion and outlook

In the course of this thesis I worked on a homodyne interferometer built to detect phase shifts and perform quantum state tomography on single photons for a future implementation in the YQO experiment at the University of Bonn. The main goal was to characterize the homodyne detection setup with regard to the inherent phase stability, the visibility of the interference signal and its detection limit.

To characterize the stability of the existing interferometer, first measurements were taken by introducing a beating between the two interferometer arms with the help of an AOM. This beating signal was evaluated via the Hilbert transform to extract the relative phase drifts between the two interferometer arms, caused by disturbances such as air currents and mechanical resonances. As far as possible, those disturbances were suppressed, for which the most effective adjustments were to build an enclosure to shield the setup from air flow which improves the phase stability by a factor of 3 for the time scale on the order of $10^{(}-2)$s and to locate and exchange one especially resonating mirrormount which strongly coupled to mechanical disturbances. After each of those upgrades, an Allan deviation plot was computed and the results were compared to see the improvement of the phase stability. To work towards the goal of a homodyne detection setup the beating frequency was turned off and a phase measurement was performed. I could show that both interferometer configurations showed a very similar phase stability especially in the time regime of interest. Although the Allan deviation showed a local maximum at the critical time scales for the YQO experiment, it can be concluded that for a first implementation, a certainty of $(4.23 \pm 0.03)^\circ$ is satisfactory.

In the further development of the homodyne detection setup it would be desirable to be able to measure the phase even more accurately. Since we know that the local maximum of the Allan deviation plot is most likely caused by other mechanical resonances of the optical components in the setup, one can approach the minimization of those resonances that happen whenever a disturbance is induced, e.g. by people walking through the laboratory or even talking loudly. This could be done by insulating the box with foam that absorbs acoustic waves. Another idea is to mechanically separate the setup from the table by mounting all the elements on a separate board and placing it on the table, with dampers between the table and the posts. If one could find optical components that don't have a resonance either at a frequency corresponding to the time scale of the experiment sequence or are very stable in general, these could replace the ones that are already in use.

Regarding the signal-to-noise ratio, I could already reach values of few photons per microsecond

while still being able to distinguish the signal from the noise, here again while measuring with the heterodyne configuration. The resulting signal-to-noise ratio was still above 1 for 10-100 photons per microsecond. I found out that increasing the power of the local oscillator has an improving effect on the SNR for LO powers where we are limited to technical noise. At higher powers there is no difference to be expected. In this case, measuring with a 1 mW local oscillator displays some technical noise, which is why an intensity of 10 mW would be recommended for being sure to be limited by shot noise.

In the future it might be worth it to try to improve the SNR further, i.e. with the help of a better detector to have a better quantum efficiency on the detected signal which is rather important to not lose too much of the information one wants to obtain. An idea to improve the detection efficiency of the used photodetector is to focus the light that is reflected from the photodiodes back onto the detection area. I installed two additional mirrors that do reflect this light back and used this configuration for the SNR measurements. Nonetheless, I did not get to optimize the new SNR which is why it did not significantly improve in contrast to the data taken without the two mirrors. This optimization is an idea to be performed in a next iteration of improving the setup and working towards the implementation into the main experiment.

The characterization of the interferometer with respect to phase stability and detection limit is an important step towards the use of this setup for homodyne tomography in the YQO experiment. To be able to measure even smaller phase shifts inherited by photons crossing the atomic cloud, in a next step, working on the stability against acoustic and mechanical perturbations and increasing the effective quantum efficiency will be of interest. This will allow to reconstruct the full quantum state of the photons which is crucial for the study of photon-photon interactions for future applications in quantum technologies.

# Bibliography


[1] O. Firstenberg, C. S. Adams and S. Hofferberth,
*Nonlinear quantum optics mediated by Rydberg interactions*,
J. Phys. B: At. Mol. Opt. Phys **49** (2016).

[2] D. Tiarks, S. Schmidt-Eberle, T. Stolz, G. Rempe and S. Dürr,
*A Photon-Photon Quantum Gate Based on Rydberg Interactions*, Nature Physics **15** (2019) 124.

[3] A. Paris-Mandoki et al., *Free-Space Quantum Electrodynamics with a Single Rydberg Superatom*,
Physical Review X **7** (2017).

[4] U. Leonhardt and H. Paul, *Measuring the Quantum States of Light*,
Progress in Quantum Electronics **19** (1995) 89.

[5] V. Magro, J. Vaneecloo, S. Garcia and A. Ourjoumtsev,
*Deterministic freely propagating photonic qubits with negative Wigner functions*,
Nature Photonics **17** (2023) 688.

[6] A. I. Lvovsky and M. G. Raymer, *Continous-variable optical quantum state tomography*,
Rev. Mod. Phys **81** (2009) 299, (visited on 14/03/2024).

[7] A. Ourjoumtsev, *Homodyne spectroscopy of a coupled cavity-atom system*, tech. rep., 2014.

[8] W. Ströbel, *Constructing a Homodyne Detector for 399nm Laser light*,
Bachelor: University of Bonn, 2023.

[9] M. Kleinert, M. E. G. Dahl and S. Bergeson, *Measurement of the Yb I 1 S0 - 1 P1 transition frequency at 399 nm using an optical frequency comb*, Physical Review A **94** (2016) 052511.

[10] T. M. Weber et al.,
*Mesoscopic Rydberg-blockaded ensembles in the superatom regime and beyond*,
Nature Phys. **11** (2015) 157.

[11] F. W. King, *Hilbert transforms*, vol. 1, Encyclopedia of Mathematics and its Applications,
Cambridge University Press, 2009.

[12] F. W. King, *Hilbert transforms*, vol. 2, Encyclopedia of Mathematics and its Applications,
Cambridge University Press, 2009.

[13] A. E. Wallin, *Implemented statistics functions*, 2023, (visited on 19/03/2024).

[14] P. Meystre and M. Sargent III, *Elements of Quantum Optics*,
Springer-Verlag Berlin Heidelberg, 2007.

[15] M. G. Raymer and M. Beck,
"Experimental quantum state tomography of optical fields and ultrafast statistical sampling",
vol. 649, Lect. Notes Phys. Springer-Verlag Berlin Heidelberg, 2004 235.

[16] H. P. Yuen and V. W. S. Chan, *Noise in homodyne and heterodyne detection*, Optics Letters **8** (1983) 177.

[17] M. J. Collett, R. Loudon and C. W. Gardiner, *Quantum Theory of Optical Homodyne and Heterodyne Detection*, Journal of Modern Optics **34** (1987) 881.